Molecular Crystals and Liquid Crystals

ISSN: 1542-1406 (Print) 1563-5287 (Online) Journal homepage: http://www.tandfonline.com/loi/gmcl20

Synthesis and Characterization of a New Series of Paramagnetic Ferroelectric Liquid Crystalline Nitroxide Radicals

Yoshiaki Uchida, Rui Tamura, Katsuaki Suzuki, Hiroki Takahashi, Yoshio Aoki & Hiroyuki Nohira

To cite this article: Yoshiaki Uchida, Rui Tamura, Katsuaki Suzuki, Hiroki Takahashi, Yoshio Aoki & Hiroyuki Nohira (2015) Synthesis and Characterization of a New Series of Paramagnetic Ferroelectric Liquid Crystalline Nitroxide Radicals, Molecular Crystals and Liquid Crystals, 615:1, 89-106, DOI: 10.1080/15421406.2015.1066966

To link to this article: http://dx.doi.org/10.1080/15421406.2015.1066966

Published online: 21 Aug 2015.

Mol. Cryst. Liq. Cryst., Vol. 615: pp. 89–106, 2015

ISSN: 1542-1406 print/1563-5287 online
DOI: 10.1080/15421406.2015.1066966

Synthesis and Characterization of a New Series of Paramagnetic Ferroelectric Liquid Crystalline Nitroxide Radicals

YOSHIAKI UCHIDA,[1,2,*] RUI TAMURA,[3] KATSUAKI SUZUKI,[3] HIROKI TAKAHASHI,[3] YOSHIO AOKI,[4] AND HIROYUKI NOHIRA[4]

[1]Graduate School of Engineering Science, Osaka University, Toyonaka, Osaka, Japan
[2]PRESTO, Japan Science and Technology Agency (JST), Kawaguchi, Saitama, Japan
[3]Graduate School of Human and Environmental Studies, Kyoto University, Kyoto, Japan
[4]Faculty of Engineering, Department of Applied Chemistry, Saitama University, Saitama, Japan

A new series of all-organic liquid-crystalline (LC) chiral radical compounds, trans-*1-alkoxyphenyl-4-[(4-(4-alkoxyphenyl)-2,5-dimethylpyrrolidine-1-oxy-2-yl)-benzylideneamino]benzenes (**1**) with various alkyl chains, containing a chiral nitroxide unit in the mesogen core were synthesized and their LC properties were fully characterized. The enantiomerically enriched compounds (2S,5S)-**1** showed N*, TGBA*, SmA* and SmC* phases, while the racemates (±)-**1** exhibited N, SmA and SmC phases. The phase transition behavior and the ferroelectric properties of the SmC* phase of (2S,5S)-**1** differed from those of previously reported analogues with an ester group as a substitute for the imino group of (2S,5S)-**1**. Some of the (2S,5S)-**1** series showed a temperature-dependent spontaneous polarization P_S (θ) inversion. We discuss the origin of this difference in terms of their molecular structures optimized by molecular orbital calculations. The phase transition behavior supports the hypothesis that the large φ, which is defined as the angle between the molecular long axis (one of the principal axes of inertia) and the direction of the dipole moment in each molecule, results in the stabilization of the SmA* (SmA) phase.*

Keywords Paramagnetic chiral liquid crystals; smectic liquid crystals; ferroelectricity; nitroxide radicals; spontaneous polarization inversion

Introduction

Nitroxides have been used as co-oxidants, [1] spin-labels, [2] spin-probes, [3] MRI contrast agents, [4] antioxidants, [5] and double sensor molecules, [6] because of (i) the thermodynamic stability of the free radical species originating from the delocalization of the unpaired

*Address correspondence to Yoshiaki Uchida, Graduate School of Engineering Science, Osaka University, Toyonaka, Osaka 560-8531, Japan. E-mail: yuchida@cheng.es.osaka-u.ac.jp

Color versions of one or more of the figures in the article can be found online at www.tandfonline.com/gmcl.

electron over the N–O bond and (ii) the unique redox properties of a nitroxyl group. Another important feature of the nitroxyl group is the possession of a large electric dipole moment (∼3 Debye) along the N–O bond [7]. Focusing on such unique magnetic, electronic and electric characteristics of the nitroxide radical, we synthesized the all-organic chiral LC radical compounds, which contain a chiral cyclic-nitroxide unit and an ester group in the mesogen core, in both enatiomerically enriched and racemic forms [8–12]. Furthermore, some of them showed a chiral smectic C (SmC*) phase in the bulk state and a ferroelectricity in a thin sandwich cell; they are the first examples of magnetic ferroelectric liquid crystals (FLCs) containing no paramagnetic metal ion [9, 10, 12]. Recently, we have reported a new chiral paramagnetic liquid crystalline compound (2*S*,5*S*)-**1i** (Fig. 1), *trans*-1-dodecyloxyphenyl-4-[(4-(4-dodecyloxyphenyl)-2,5- dimethylpyrrolidine-1-oxy-2-yl)benzylideneamino]benzene, which has a cyclic nitroxide radical moiety and shows chiral smectic A (SmA*) and SmC* phases [13]. The compound shows pretransitional layer contraction prior to the SmA*-to-SmC* phase transition in the cooling run, which has not been observed for previously reported analogue compounds (2*S*,5*S*)-**2** and (2*S*,5*S*)-**3** (Fig. 1).

To gain an insight into the origin of this difference in terms of their molecular structures, we have synthesized a series of analogues racemic and (2*S*,5*S*)-**1** with C4 to C13 alkyl chains (Fig. 1). Here we report the LC phase transition behavior of racemic and (2*S*,5*S*)-**1** and the ferroelectricity of (2*S*,5*S*)-**1**, and compare them with those of compounds **2** and **3**.

Experimental

Unless otherwise noted, solvents and reagents were reagent grade and used without further purification. Tetrahydrofuran (THF) which is used for electron paramagnetic resonance (EPR) spectral measurement or Grignard reactions was distilled from

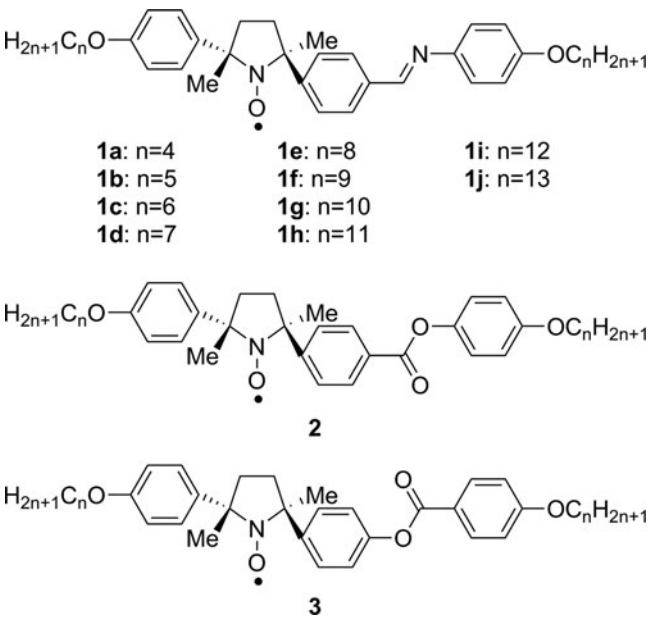

Figure 1. Molecular structures of (2*S*,5*S*)-**1**, (2*S*,5*S*)-**2** and (2*S*,5*S*)-**3**.

sodium/benzophenone ketyl under argon. Phase transition temperatures were determined by DSC (SHIMADZU DSC-50) and POM (Olympus BHSP). Hot-stage (JHC TH-600PH) was used as the temperature control unit for the microscopy. IR spectra were recorded with SHIMADZU IRPrestige-21. EPR spectra were recorded with a JEOL FE1XG. For variable-temperature XRD measurement, the data collections were performed on a Rigaku RINT2200/PC-LH diffractometer.

Synthesis of 1

The synthesis of racemic and (2*S*,5*S*)-**1** is presented in Scheme 1. They were prepared from racemic or (*R*)-**4**.

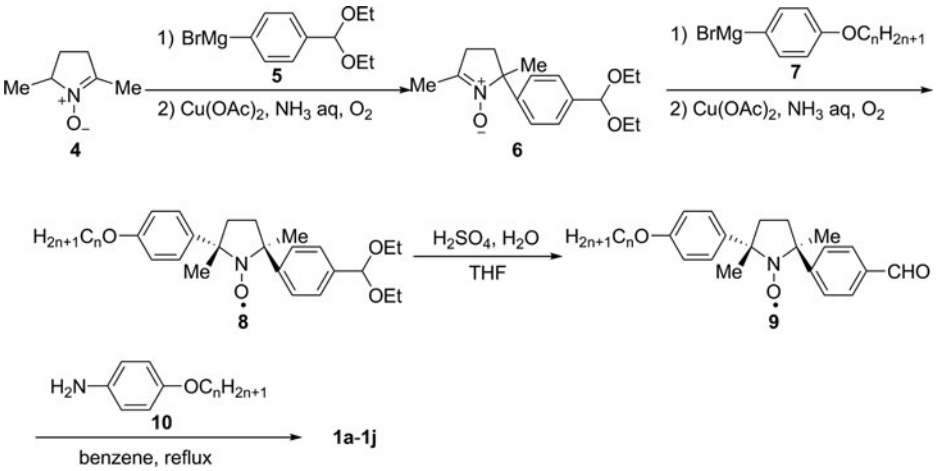

Scheme 1. Synthesis of compound **1**.

Synthesis of 4-Alkoxy-1-bromobenzene used for the synthesis of 7

A mixture of 4-bromophenol (50 mmol), DMF (70 ml) and potassium carbonate (100 mmol) was stirred at 70°C for 0.5 h. To the suspension was added alkyl iodide (50 mmol) and the mixture was stirred at 70°C overnight. Water (200 ml) was added and the mixture was extracted with hexane. The organic extracts were washed with brine (50 ml), 1N NaOH solution (50 ml) and water (100 ml), dried over $MgSO_4$, and evaporated to give 4-alkoxy-1-bromobenzene (> 90%).

Synthesis of Aryl magnesium bromides 5, 7 [8–19]

To magnesium turnings (0.243 g, 10 mmol) dried by heating at 3 mmHg were added THF (10 ml), arylbromide (10 mmol), and a small amount of iodine under argon. The reaction started by heating, and the reaction mixture was refluxed for 4 h to afford a solution of aryl magnesium bromide **5** and **7** in THF.

General synthetic procedure for (±)-1 and (2S,5S)-1 [8–21]

To a solution of the nitrone **4** (5.0 mmol) in THF (10 ml) was slowly added a stirred solution of the freshly prepared Grignard reagent **5** (10 mmol) in THF under argon at –78°C [8–19]. The temperature was raised slowly to room temperature, and stirring was continued overnight. The reaction mixture was poured into a saturated aqueous NH_4Cl solution (50 ml), and then extracted with dichloromethane (DCM) (2 × 50 ml). The combined DCM extract was dried over $MgSO_4$ and evaporated. The residual oil was dissolved in methanol (20 ml). To this solution were added aqueous NH_3 solution (25 wt%, 1.4 ml) and copper (II) acetate monohydrate (0.160 g, 0.80 mmol). Oxygen was bubbled through the yellow solution until a persistent deep blue color was observed. The solvent was then removed under reduced pressure and the crude product was dissolved in DCM (50 ml). This solution was washed with saturated aqueous $NaHCO_3$ (50 ml) and dried over $MgSO_4$, and the solvent removed under reduced pressure. The residue was dried by azeotropic removal of water with benzene, followed by removal of the remaining benzene at 3 mmHg. The crude acetal **6** was dissolved in THF (10 ml) and reacted with the freshly prepared Grignard reagent **7** (the same quantity and conditions as described above). After a similar workup procedure, the crude product was again oxidized by O_2/copper acetate. The crude nitroxide radical **8** was purified by column chromatography (hexane/ether = 17/3) on silica gel. To a solution of **8** in THF (2 ml) was added aqueous H_2SO_4 (5%; 0.50 ml) and the mixture was stirred for 8 h at 25°C. Brine and DCM were then added. The organic phase was separated and dried over $MgSO_4$, and the solvent was evaporated under reduced pressure to provide 2-(4-alkyloxyphenyl)-5-(4-formylphenyl)-2,5-dimethylpyrrolidine-1-oxy (**9**). To a solution of **9** (0.31 mmol) in benzene (20 ml) was added 4-alkoxyaniline **10**[20, 21] and the mixture was refluxed by using Dean-Stark trap overnight. The reaction mixture was evaporated and purified by column chromatography (hexane/ethyl acetate = 4/1) on silica gel to afford the imine **1** (1∼10% yield from **4**). The *ee* values of (2*S*,5*S*)-**1** were determined by HPLC analysis.

(±)-*trans*-1-Butoxyphenyl-4-[(4-(4-butoxyphenyl)-2,5-dimethylpyrrolidine-1-oxy-2-yl) benzylideneamino]benzene (**1a**). Found: C, 77.38; H, 7.98; N, 5.62. Calc. for $C_{33}H_{41}N_2O_3$: C, 77.16; H, 8.04; N, 5.45%. ν_{max}(KBr)/cm^{-1} 2962, 2933, 2672, 1624, 1609, 1510, 1247, and 837. EPR: $g = 2.0057$, $a_N = 1.33$ mT. 3% yield from (±)-**4**.

*(2S,5S)-**1a** (85% ee). [α]$^{14}_D$ –107.7° (c 0.075 in THF). 5% yield from (*R*)-**4**.*

(±)-*trans*-1-Pentyloxyphenyl-4-[(4-(4-pentyloxyphenyl)-2,5-dimethylpyrrolidine-1-oxy-2-yl)benzylideneamino]benzene (**1b**). Found: C, 77.69; H, 8.24; N, 5.15. Calc. for $C_{34}H_{45}N_2O_3$: C, 77.60; H, 8.37; N, 5.17%. ν_{max}(KBr)/cm^{-1} 2949, 2932, 2864, 1622, 1609, 1508, 1474, and 837. EPR: $g = 2.0060$, $a_N = 1.34$ mT. 2% yield from (±)-**4**.

*(2S,5S)-**1b** (81% ee). [α]$^{14}_D$ –97.4° (c 0.046 in THF). 5% yield from (*R*)-**4**.*

(±)-*trans*-1-Hexyloxyphenyl-4-[(4-(4-hexyloxyphenyl)-2,5-dimethylpyrrolidine-1-oxy-2-yl)benzylideneamino]benzene (**1c**). Found: C, 77.94; H, 8.65; N, 4.78. Calc. for $C_{37}H_{49}N_2O_3$: C, 77.99; H, 8.67; N, 4.92%. ν_{max}(KBr)/cm^{-1} 2951, 2927, 2860, 1623, 1608, 1508, 1470, 1247, and 839. EPR: $g = 2.0060$, $a_N = 1.34$ mT. 3% yield from (±)-**4**.

*(2S,5S)-**1c** (86% ee). [α]$^{14}_D$ –106.8° (c 0.198 in THF). 9% yield from (*R*)-**4**.*

(±)-*trans*-1-Heptyloxyphenyl-4-[(4-(4-heptyloxyphenyl)-2,5-dimethylpyrrolidine-1-oxy-2-yl)benzylideneamino]benzene (**1d**). Found: C, 78.36; H, 8.92; N, 4.68. Calc. for

$C_{37}H_{49}N_2O_3$: C, 78.35; H, 8.94; N, 4.69%. ν_{max}(KBr)/cm^{-1} 2956, 2926, 2856, 1623, 1606, 1508, 1468, 1250, and 838. EPR: $g = 2.0059$, $a_N = 1.33$ mT. 2% yield from (±)-**4**.

*(2S,5S)-**1d** (75% ee). [α]$^{14}_D$ –76.4° (c 0.066 in THF). 3% yield from (*R*)-**4**.*
(±)-*trans*-1-Octyloxyphenyl-4-[(4-(4-octyloxyphenyl)-2,5-dimethylpyrrolidine-1-oxy-2- yl)benzylideneamino]benzene (**1e**). Found: C, 78.48; H, 9.25; N, 4.34. Calc. for $C_{37}H_{49}N_2O_3$: C, 78.68; H, 9.18; N, 4.48%. ν_{max}(KBr)/cm^{-1} 2954, 2918, 2850, 1624, 1607, 1509, 1467, 1247, and 837. EPR: $g = 2.0061$, $a_N = 1.33$ mT. 4% yield from (±)-**4**.

*(2S,5S)-**1e** (91% ee). [α]$^{14}_D$ –79.7° (c 0.050 in THF). 7% yield from (*R*)-**4**.*
(±)-*trans*-1-Nonyloxyphenyl-4-[(4-(4-nonyloxyphenyl)-2,5-dimethylpyrrolidine-1-oxy-2-yl)benzylideneamino]benzene (**1f**). Found: C, 78.93; H, 9.46; N, 4.26. Calc. for $C_{43}H_{61}N_2O_3$: C, 78.97; H, 9.40; N, 4.28%. ν_{max}(KBr)/cm^{-1} 2955, 2923, 2854, 1624, 1606, 1508, 1468, 1247, and 838. EPR: $g = 2.0061$, $a_N = 1.33$ mT. 4% yield from (±)-**4**.

*(2S,5S)-**1f** (89% ee). [α]$^{14}_D$ –94.1° (c 0.067 in THF). 4% yield from (*R*)-**4**.*
(±)-*trans*-1-Decyloxyphenyl-4-[(4-(4-decyloxyphenyl)-2,5-dimethylpyrrolidine-1-oxy-2-yl)benzylideneamino]benzene (**1g**). Found: C, 79.42; H, 9.70; N, 4.13. Calc. for $C_{45}H_{65}N_2O_3$: C, 79.25; H, 9.61; N, 4.11%. ν_{max}(KBr)/cm^{-1} 2954, 2921, 2852, 1621, 1607, 1509, 1474, 1249, and 836. EPR: $g = 2.0061$, $a_N = 1.34$ mT. 5% yield from (±)-**4**.

*(2S,5S)-**1g** (83% ee). [α]$^{14}_D$ –85.4° (c 0.098 in THF). 2% yield from (*R*)-**4**.*
(±)-*trans*-1-Undecyloxyphenyl-4-[(4-(4-undecyloxyphenyl)-2,5-dimethylpyrrolidine-1-oxy-2-yl)benzylideneamino]benzene (**1h**). Found: C, 79.44; H, 10.04; N, 3.82. Calc. for $C_{47}H_{69}N_2O_3$: C, 79.50; H, 9.79; N, 3.95%. ν_{max}(KBr)/cm^{-1} 2956, 2920, 2851, 1622, 1607, 1509, 1473, 1250, and 836. EPR: $g = 2.0060$, $a_N = 1.33$ mT. 1% yield from (±)-**4**.

*(2S,5S)-**1h** (89% ee). [α]$^{14}_D$ –91.4° (c 0.095 in THF). 16% yield from (*R*)-**4**.*
(±)-*trans*-1-Dodecyloxyphenyl-4-[(4-(4-dodecyloxyphenyl)-2,5-dimethylpyrrolidine-1-oxy-2-yl)benzylideneamino]benzene (**1i**). Found: C, 79.60; H, 9.76; N, 3.74. Calc. for $C_{49}H_{73}N_2O_3$: C, 79.73; H, 9.97; N, 3.80%. ν_{max} (KBr)/cm^{-1} 2955, 2921, 2851, 1625, 1606, 1509, 1469, 1245, and 838. EPR: $g = 2.0061$, $a_N = 1.33$ mT. 7% yield from (±)-**4**.

*(2S,5S)-**1i** (85% ee). [α]$^{14}_D$ –50.6° (c 0.086 in THF). 6% yield from (*R*)-**4**.*
(±)-*trans*-1-Tridecyloxyphenyl-4-[(4-(4-tridecyloxyphenyl)-2,5-dimethylpyrrolidine-1-oxy-2-yl)benzylideneamino]benzene (**1j**). Found: C, 79.89; H, 10.27; N, 3.59. Calc. for $C_{51}H_{77}N_2O_3$: C, 79.95; H, 10.13; N, 3.66%. ν_{max}(KBr)/cm^{-1} 2955, 2919, 2851, 1625, 1607, 1510, 1470, 1247, and 836. EPR: $g = 2.0060$, $a_N = 1.33$ mT. 8% yield from (±)-**4**.

Measurements

High-performance liquid chromatographic (HPLC) analysis was performed using a chiral stationary phase column (Daicel Chiralcel OD-H, 0.46 cm x 25 cm), a mixture of hexane and 2-propanol (9:1) as the mobile phase at a flow rate of 1.0 mL min^{-1}, and an UV-vis spectrometer (254 nm) as the detector. X-Band EPR spectra were measured in THF at 25°C

Table 1. Phase transition temperatures (°C) and transition enthalpies (in parentheses, kJ/mol) of racemic **1a**-**1j**

Compounds	Phase transition temperature (°C) (transition enthalpy (kJ/mol))
(±)-**1a** (n = 4)	Cr 133 (-)[a] Cr 137 (-)[a] N 165 (2.3) Iso : heating
	Iso 163 (6.3) N [< 25][b] Cr : cooling
(±)-**1b** (n = 5)	Cr 129 (43.8) N 148 (1.4) Iso : heating
	Iso 146 (1.0) N 53 (7.6) Cr : cooling
(±)-**1c** (n = 6)	Cr 109 (27.8) N 134 (1.7) Iso: heating
	Iso 130 (1.4) N 67 (21.9) Cr: cooling
(±)-**1d** (n = 7)	Cr 109 (31.2) N 130 (1.6) Iso : heating
	Iso 126 (1.5) N 73 (19.9) Cr : cooling
(±)-**1e** (n = 8)	Cr 101 (27.1) N 127 (2.2) Iso : heating
	Iso 125 (2.3) N 79 (24.9) Cr : cooling
(±)-**1f** (n = 9)	Cr 96 (22.4) SmA 109 (0.50) N 118 (1.8) Iso: heating
	Iso 115 (2.0) N 106 (0.28) SmA 89 (-)[c] SmC 70 (19.7) Cr: cooling
(±)-**1g** (n = 10)	Cr 98 (28.1) SmA 119 (5.3) Iso: heating
	Iso 115 (2.8) SmA 97 (-)[c] SmC 75 (18.0) Cr: cooling
(±)-**1h** (n = 11)	Cr 96 (27.6) SmA 113 (7.3) Iso: heating
	Iso 110 (5.6) SmA 88 (-)[c] SmC 67 (21.5) Cr: cooling
(±)-**1i** (n = 12)	Cr 93 (26.2) SmC 97 (-)[c] SmA 118 (7.9) Iso: heating
	Iso 114 (6.7) SmA 94 (-)[c] SmC 72 (24.0) Cr: cooling
(±)-**1j** (n = 13)	Cr 91 (29.0) SmC 97 (-)[c] SmA 116 (9.0) Iso: heating
	Iso 113 (8.5) SmA 95 (-)[c] SmC 72 (27.9) Cr: cooling

[a]Two peaks are overlapping so that the transition enthalpies are united.
[b]The transition from the nematic phase to the crystalline phase occurs below room temperature.
[c]The phase transition is not observed by DSC but by POM.

under an applied magnetic field of 0.34 T. The variable temperature XRD patterns were recorded at a continuous scanning rate of 2° 2θ min^{-1} and at a heating or cooling rate of 4 °C min^{-1} using Cu Kα radiation (40 kV, 40 mA), with the intensity of diffracted X-rays being collected at intervals of 0.02° 2θ. DSC was performed at a scanning rate of 5°C min^{-1}. The magnitude of spontaneous polarization, P_S, was determined by using 4 μm cells with indium tin oxide (ITO) electrodes coated with polyimide in an electric field of 20 V (5.0 V μm^{-1}) at a frequency of 20 Hz for (2*S*,5*S*)-**1**. The tilt angle (θ) was measured as a function of the temperature between crossed Nicol polarisers under an applied direct-current (DC) electric field of 2.5 V μm^{-1}, and was recorded as half the rotation angle between the two extinction positions associated with the oppositely directed polarization. For the X-ray crystallographic analysis of (±)-**1a**, the single crystal was mounted in a sealed capillary. The single crystal of (±)-**1a** appropriate for X-ray analysis was obtained by crystallization from hexane/DCM. The data collections were performed at 173 K on a Rigaku RAXIS RAPID diffractometer with graphite monochromated Mo-Kα radiation to $2\theta_{max}$ of 55.0°. All of the crystallographic calculations were performed by using the CrystalStructure 3.6.0 of Rigaku and Rigaku/MSC. The crystal structure was solved by direct methods and refined by using full-matrix least squares. All non-hydrogen atoms were refined anisotropically. The X-ray crystal structure of (±)-**1a** is shown in Fig. A1 in the Appendix. Crystallographic data (excluding structure factors) for the structure have been deposited with the Cambridge Crystallographic Data Center (CCDC-685828). Copies of the data can be obtained, free

Table 2. Phase transition temperatures (°C) and transition enthalpies (in parentheses, kJ/mol) of enantiomerically enriched **1a–1j**

Compounds	*ee* (%)	Phase transition temperature (°C) (transition enthalpy (kJ/mol))
(2*S*,5*S*)-**1a** (n = 4)	85	Cr 112 (22.7) N* 159 (2.1) Iso: heating Iso 151 (0.1) N* [< 25][a] Cr: cooling
(2*S*,5*S*)-**1b** (n = 5)	81	Cr 105 (3.7) N* 132 (1.9) Iso: heating Iso 128 (2.0) N* [< 25][a] Cr: cooling
(2*S*,5*S*)-**1c** (n = 6)	86	Cr 64 (18.0) N* 128 (1.7) Iso: heating Iso 126 (1.7) N* [< 25][a] Cr: cooling
(2*S*,5*S*)-**1d** (n = 7)	75	Cr 89 (-)[b] Cr 105 (-)[b] N* 132 (1.8) Iso: heating Iso 129 (1.4) N* [< 25][a] Cr: cooling
(2*S*,5*S*)-**1e** (n = 8)	91	Cr 87 (22.5) N* 131 (1.7) Iso: heating Iso 127 (1.5) N* 40 (5.7) Cr: cooling
(2*S*,5*S*)-**1f** (n = 9)	89	Cr 81 (49.0) SmC* 90 (-)[c] SmA* 108 (0.67) [c,d] TGBA* 109 (-)[c,d] N* 118 (2.4) Iso: heating Iso 115 (2.6) N* 109 (0.45)[c,d] TGBA* 108 (-)[c,d] SmA* 83 (-)[c] SmC* 46 (24.1) Cr: cooling
(2*S*,5*S*)-**1g** (n = 10)	83	Cr 94 (56.0) SmA* 118 (6.73)[d] TGBA*[e] 118 (-)[c,d] N* 120 (-)[c,d] Iso: heating Iso 117 (6.26)[d] N* 114 (-)[c,d] TGBA*[e] 114 (-)[c,d] SmA* 84 (-)[c] SmC* 42 (31.8) Cr: cooling
(2*S*,5*S*)-**1h** (n = 11)	89	Cr 95 (43.0) SmA* 118 (6.0) Iso: heating Iso 115 (5.1) SmA* 85 (-)[c] SmC* 48 (35.6) Cr: cooling
(2*S*,5*S*)-**1i** (n = 12)	85	Cr 89 (35.7) SmA* 118 (5.6) Iso: heating Iso 115 (4.7) SmA* 89 (-)[c] SmC* 46 (22.4) Cr: cooling
(2*S*,5*S*)-**1j** (n = 13)	86	Cr 84 (40.5) SmC* 96 (-)[c] SmA* 116 (8.7) Iso: heating Iso 113 (7.8) SmA* 94 (-)[c] SmC* 49 (34.9) Cr: cooling

[a]Two peaks are overlapping so that the transition enthalpies are united.
[b]The transition from the nematic phase to the crystalline phase occurs below room temperature.
[c]The phase transition is not observed by DSC but by POM (Fig. S2).
[d]Transition enthalpies were unable to be determined.
[e]This phase was observed only between the oily-streak texture of the N* phase and the fan-shaped of the SmA* phase by POM.

of charge, on application to the Director, CCDC, 12 Union Road, Cambridge CB2 1EZ, UK (Fax: +44-1223-336033 or e-mail: deposit@ccdc.cam.ac.uk). The summary of the fundamental crystal data and experimental parameters for the structure solution is given in Table A1 in the Appendix.

Table 3. Layer distances *d* from XRD of (±)-**1f**-**j** ((2*S*,5*S*)-**1f**-**j**) in the SmA (SmA*) and SmC (SmC*) phases[a]

Compound [*ee* (%)]	XRD *d* (Å)	
	SmA or SmA* phases	SmC or SmC* phases
(±)-**1f** (n = 9)	38.9 (100°*C*)	38.3 (80°*C*)
(2*S*,5*S*)-**1f** [89]	37.1 (100°*C*)	35.7 (75°*C*)
(±)-**1g** (n = 10)	40.7 (100°*C*)	39.8 (85°*C*)
(2*S*,5*S*)-**1g** [83]	38.5 (110°*C*)	36.2 (50°*C*)
(±)-**1h** (n = 11)	42.8 (95°*C*)	42.8 (85°*C*)
(2*S*,5*S*)-**1h** [89]	40.5 (110°*C*)	39.2 (70°*C*)
(±)-**1i** (n = 12)	44.1 (104°*C*)	43.5 (85°*C*)
(2*S*,5*S*)-**1i** [85]	41.6 (100°*C*)	39.8 (70°*C*)
(±)-**1j** (n = 13)	46.5 (105°*C*)	46.0 (85°*C*)
(2*S*,5*S*)-**1j** [86]	44.6 (96°*C*)	45.0 (70°*C*)

[a] On the cooling run.

Results and Discussion

The phase transition behaviors of compounds **1** were characterized by differential scanning calorimetry (DSC), polarized optical microscopy (POM), and X-ray diffraction (XRD) analysis (Table 1–3, Fig. 2–4).

Generally, (±)-**1** showed higher crystal-to-LC transition and clearing temperatures than those of (±)-**2** with the same alkyl chains, most likely due to their higher stability in both the crystalline and LC states of (±)-**1** (Fig. 2a). Racemic **1a**–**1e** with C4–C8

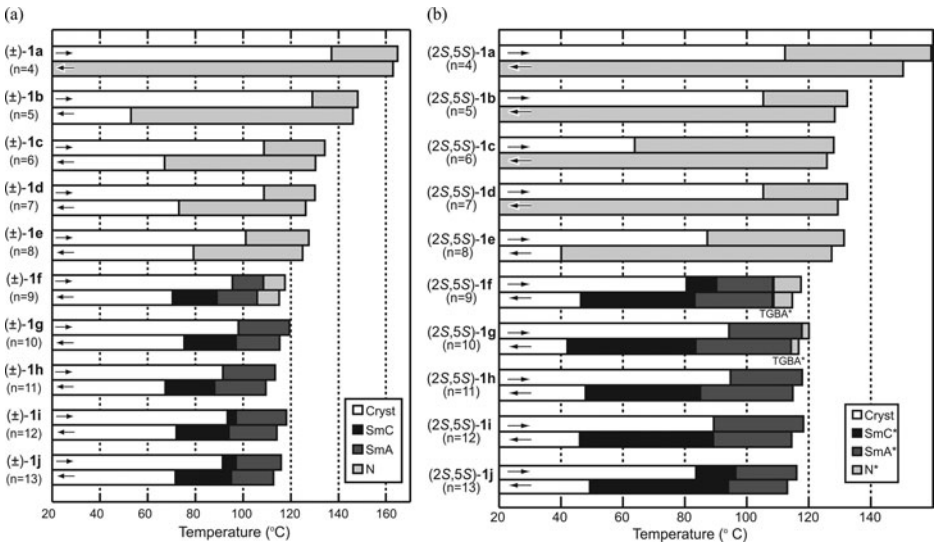

Figure 2. Liquid crystalline behaviour of (a) (±)-**1** and (b) (2*S*,5*S*)-**1**: transition temperatures determined by DSC and POM on the heating (upper bar) and cooing (lower bar) runs.

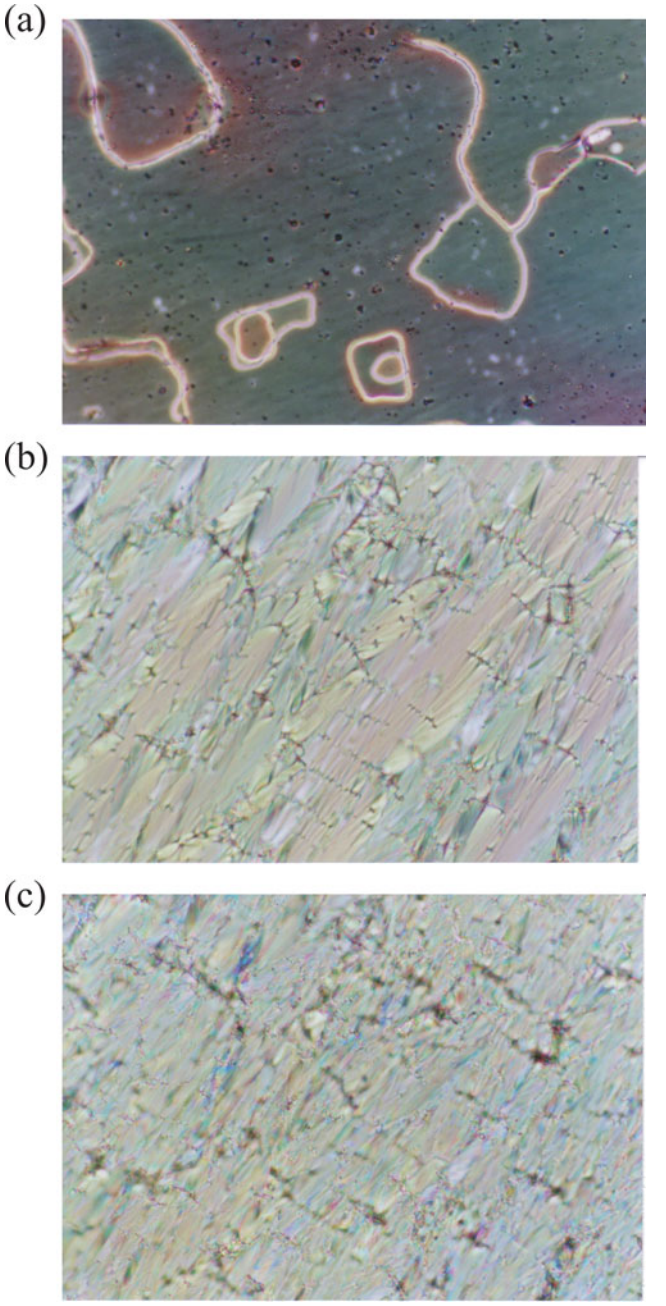

Figure 3. Polarized optical microphotographs of (±)-**1** on the cooling run: (a) a thread-like texture for the N phase of (±)-**1c** at 113.3°C; (b) a fan-shaped texture for the SmA phase of (±)-**1j** at 104.9°C; (c) a broken fan-shaped texture for SmC phase of (±)-**1j** at 85.0°C. All textures were observed under homogeneous planar boundary conditions in a thin-sandwich LC cell (25 μm thickness and 50 μm thickness for (±)-**1c** and (±)-**1j**, respectively) consisting of two glass plates covered with antiparallel-rubbed polyimide films.

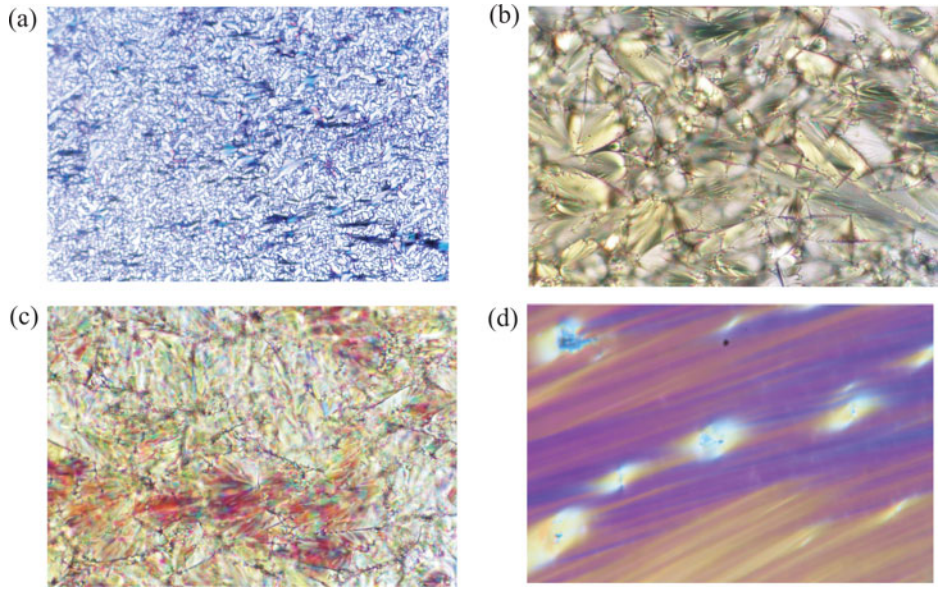

Figure 4. Polarized optical microphotographs of (2*S*,5*S*)-**1**: (a) a fan-like texture for the N* phase of (2*S*,5*S*)-**1f** at 110.0°C on the cooling run; (b) a fan-shaped texture for SmA* phase of (2*S*,5*S*)-**1j** at 110.0°C on the cooling run; (c) a broken fan-shaped texture for the SmC* phase of (2*S*,5*S*)-**1j** at 75.0°C on the cooling run; (d) a blurred fan-shaped texture for the TGBA* phase of (2*S*,5*S*)-**1f** at 108.7°C on the heating run. Texture (a) was observed under random conditions, while other textures were observed under homogeneous planar boundary conditions in a thin-sandwich LC cell (4 μm thickness and 50 μm thickness for (2*S*,5*S*)-**1f** and (2*S*,5*S*)-**1j**, respectively) consisting of two glass plates covered with antiparallel-rubbed polyimide films.

chains showed only an enantiotropic N phase, while no odd-even effect of alkyl chains was noted. Racemic **1f**, **1g**, and **1h** with C9–C11 chains showed SmA and monotropic SmC phases, while enantiotropic SmA and SmC phases were observed for (±)-**1i** and (±)-**1j** with C12 and C13 chains. The N—SmA transition for (±)-**1f** was accompanied by very small enthalpy changes (0.50 and 0.28 kJ/mol on the heating and cooling runs, respectively) (Table 1). A typical thread-like texture, a fan-shaped texture and a broken fan-shaped one were observed for these N, SmA and SmC phases by POM, respectively (Fig. 3). Variable temperature XRD analysis verifies the existence of these smectic phases (Table 3).

The phase transition behavior of (2*S*,5*S*)-**1** was quite different from that of the corresponding (±)-**1** (Fig. 2b). Namely, (2*S*,5*S*)-**1** exhibited a wider temperature range of the SmC* phase than that of the SmC phase of (±)-**1**. As to the optical texture by POM, (2*S*,5*S*)-**1a**–**1f** with C4–C9 chains exhibited a fan-like texture which is typical of N* phase, respectively, on the cooling run (Fig. 4a), while (2*S*,5*S*)-**1f**–**1j** with C9–C13 chains did fan-shaped and broken fan-shaped textures which are typical of SmA* and SmC* phases, respectively, on the cooling run (Fig. 4b, c). Interestingly, (2*S*,5*S*)-**1f** with C9 chains showed not only N*, SmA* and SmC* phases but also a TGBA* phase with a blurred fan-shaped or Granjean texture in a very narrow temperature range (0.3∼0.4°) between the N* and SmA* phases on the cooling run (Fig. 4d). The N*-to-TGBA* transition for (2*S*,5*S*)-**1f** was accompanied by very small enthalpy changes (less than 0.45 kJ/mol) (Table 2). (2*S*,5*S*)-**1g** with C10 chains also showed a TGBA* phase; this unstable phase was observed between

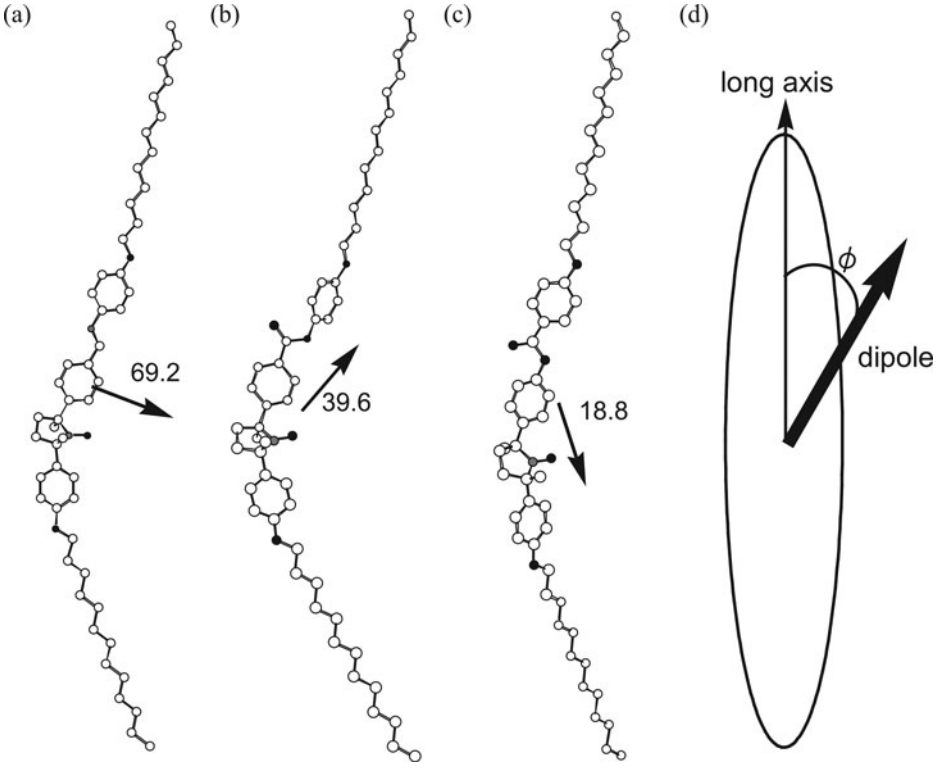

Figure 5. The molecular conformations of (a) **1j,** (b) **2** (n = 13) and (c) **3** (n = 13) optimized by the unrestricted AM1 method (PC Spartan'02), and (d) the schematic representation of the angle ϕ between the molecular long axis and the direction of the dipole moment. Arrows show the direction of each dipole moment.

the oily-streak texture of the N* phase and the fan-shaped texture of the SmA* phase only by POM. Variable temperature XRD analysis verifies the existence of these smectic phases (Table 3).

In order to shed light on the difference in the phase transition behavior of **1**, **2** and **3**, each of their molecular dipole moments was calculated for (2*S*,5*S*)-**1j**, (2*S*,5*S*)-**2** (n = 13) and (2*S*,5*S*)-**3** (n = 13) with the same C13 alkyl chains. Each molecular conformation with two structurally fixed linear anti-conformational alkyl chains was optimized by the Monte Carlo method using the Merck Molecular Force Field (MMFF), followed by the AM1 semi-empirical calculation using PC Spartan'02.[22] The optimized molecular geometries have a distorted zigzag structure that is advantageous for the appearance of an SmC* phase (Fig. 5a–c).[23] The angle ϕ, which is defined as the angle between the molecular long axis (one of the principal axes of inertia) and the direction of the dipole moment in each molecule (Fig. 5d), was 69.2 (73.7), 39.6 (33.9) and 18.8 (19.5) degrees for **1j**, **2** (n = 13) and **3** (n = 13), respectively (Fig. 5a-c).

Although further investigation is necessary to know the whole aspect, the difference in the direction of dipole moment between **1j**, **2** (n = 13) and **3** (n = 13) must be responsible for the difference in the phase transition behavior; the large ϕ may stabilize the interlayer dipole interaction to direct the molecular dipole moment perpendicular to the molecular long axis

Table 4. Basic magnetic properties of **1**

	EPR		SQUID (racemate)		SQUID (2*S*,5*S*-isomer)		
Compound	*g*	a_N (mT)	*C* (emu K mol^{-1})	θ_ω (K)	*ee* (%)	*C* (emu K mol^{-1})	θ_ω (K)
1a (n = 4)	2.0057	1.33	0.398	–0.16	85	0.380	–0.52
1b (n = 5)	2.0060	1.34	0.374	–0.40	81	0.378	–0.15
1c (n = 6)	2.0060	1.34	0.381	–3.24	86	0.381	–0.19
1d (n = 7)	2.0059	1.33	0.331	–18.15	75	0.380	–0.54
1e (n = 8)	2.0061	1.33	0.384	–1.88	91	0.375	–0.47
1f (n = 9)	2.0061	1.33	0.380	–0.30	89	0.374	–0.36
1g (n = 10)	2.0061	1.34	0.349	–0.62	83	0.376	+0.11
1h (n = 11)	2.0060	1.33	0.362	–0.36	89	0.377	–0.47
1i (n = 12)	2.0061	1.33	0.362	–0.36	85	0.377	–0.56
1j (n = 13)	2.0060	1.33	0.362	+0.34	86	0.373	–0.05

and parallel to the smectic layer plane. Therefore, the stabilization of SmA (SmA*) phases for **1** and **2** can be rationalized in analogy to H-type aggregation in π-organogels.[24] For the same reason, the small ϕ for **3** favors N (N*) and SmC (SmC*) phases.

The basic magnetic properties of **1** are summarized in Table 4. The EPR spectra were measured in THF at a field of 0.34 T at 25°C, displaying a characteristic intense 1:1:1 triplet. The magnetic susceptibility was measured in a quartz tube (3.5 ϕ × 40 mm) on a SQUID magnetometer at a field of 0.5 T in the temperature range of 2-300 K. The Curie constants (*C*) thus obtained indicate that the radical purity of **1** is very high. Almost all of **1** showed very weak intermolecular antiferromagnetic interactions (Weiss constant: $\theta_W < 0$), except that only (±)-**1d** showed relatively strong antiferromagnetic interactions ($\theta_W = -18$ K). Although the crystal structure of (±)-**1d** has not been obtained yet due to the poor crystallinity, it is conceivable that the SOMO-SOMO overlapping due to a close contact between the neighboring nitroxyl groups is responsible for such relatively strong antiferromagnetic interactions.[25]

Table 5. Ferroelectric properties of (2*S*,5*S*)-1.

Compound [ee (%)]	$P_S(-10°)^a$ (nC cm^{-2})	$\tau_{10\text{-}90}$ $(-10°)^b$ (ms)	$\gamma(-10°)^c$ (m Pa s)	θ $(-10°)^d$ (deg)
(2*S*,5*S*)-**1f** [89]	6.9	0.465	91.6	17
(2*S*,5*S*)-**1g** [83]	1.9	0.650	35.2	18
(2*S*,5*S*)-**1h** [89]	6.2	0.750	133	17
(2*S*,5*S*)-**1i** [85]	5.8	0.480	79.5	17
(2*S*,5*S*)-**1j** [86]	3.7	0.465	49.2	19

[a]Spontaneous polarization.
[b]Optical response time required to attain 10–90% of the optical transmittance after field reversal.
[c]Viscosity calculated using $\gamma = |Ps|E\tau_{10\text{-}90}/1.75$ (ref 8).
[d]Optical tilt angle measured by POM.

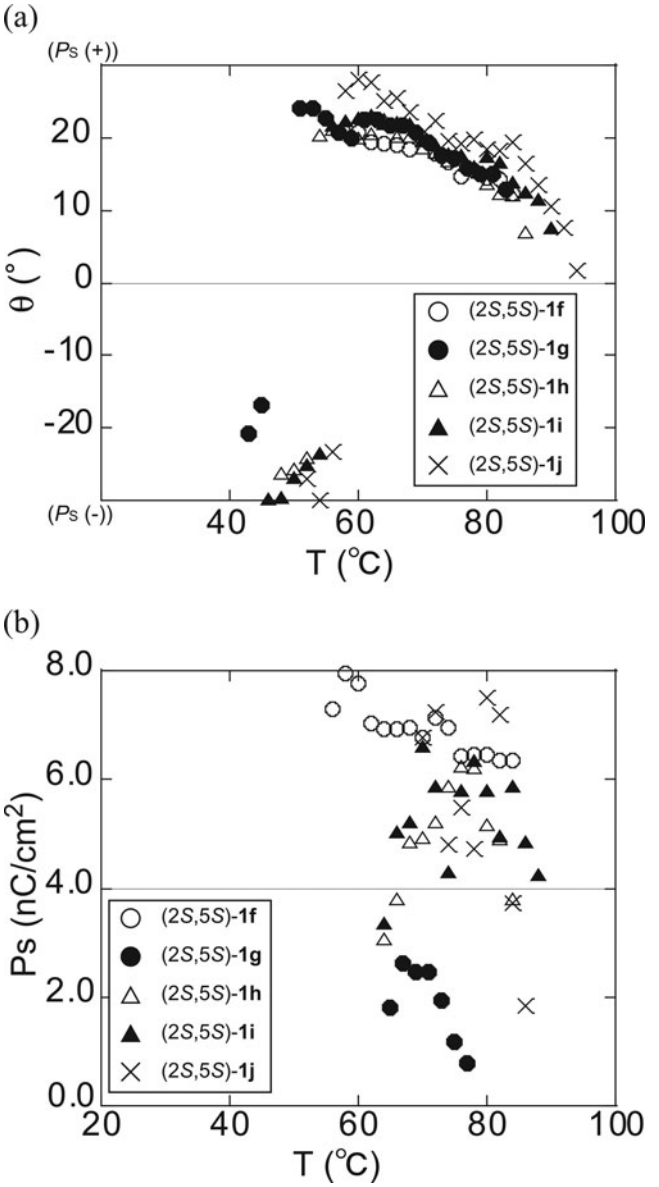

Figure 6. (a) θ and (b) P_S of (2*S*,5*S*)-**1f**-**j**.

The magnitude of the spontaneous polarization (P_S) and the tilt angle (θ) of (2*S*,5*S*)-**1f**–**1j** evaluated by POM are shown in Table 5 and Fig. 6. A temperature-dependent P_S (θ) inversion [26] was observed by measurement of θ in the SmC* phase of (2*S*,5*S*)-**1f**–**1j** (Fig. 6a). On the cooling run from the SmA*-to-SmC* transition temperature, the positive θ gradually increased, the positive-to-negative θ inversion occurred between 45 and 60°C and then the absolute value of negative θ increased (Fig. 6a). Around the transition temperature θ was unable to be measured with accuracy, because interconversion between two types of

domains with opposite signs of θ occurred. In the case of (2*S*,5*S*)-**1f**, only positive θ was observed.

The positive P_S value of (2*S*,5*S*)-**1f**, (2*S*,5*S*)-**1g**, (2*S*,5*S*)-**1h** and (2*S*,5*S*)-**1j** initially increased, reached a plateau and gradually decreased in the proximity of the θ inversion temperature on the cooling run (Fig. 6b). The peak of P_S, however, was too broad to measure below the θ inversion temperature (Fig. 6b). In the case of (2*S*,5*S*)-**1f**, the positive P_S value initially increased, reached a plateau, gradually decreased and finally was unable to be measured. We previously reported that (2*S*,5*S*)-**1i** showed an analogous P_S (θ) inversion and estimated that their inversion resulted from the temperature dependent interconversion between different conformations of the chiral mesogen core [13]. This estimation would be applicable to the other cases of (2*S*,5*S*)-**1** that exhibited a positive or a negative θ above or below 45∼60°C, respectively. This phenomenon is of little relevance to the alkyl chain length.

Conclusion

We have reported the synthesis, characterisation and ferroelectric properties of a new series of all-organic radical liquid crystals **1**. The enantiomerically enriched or racemic **1** showed N*, TGBA*, SmA* and SmC* phases, or N, SmA and SmC phases, respectively. The phase transition behaviour supports the hypothesis that the large ϕ results in the stabilization of the SmA*(SmA) phase. The stabilization of SmA (SmA*) phases for **1** and **2** can be rationalized in analogy to H-type aggregation in π-organogels. Additionally, we observed a temperature-dependent θ inversion for (2*S*,5*S*)-**1f**–**1j**. Although the origin of this P_S (θ) inversion cannot be fully explained at present, an EPR spectroscopic study of these compounds will provide further important information on the conformational change in the LC molecules.

Acknowledgment

This work was supported by the Grant-in Aid for Scientific Research (No. 19350067) from Japan Society for the Promotion of Science, the Asahi Glass Foundation (R.T.) and the Research Fellowships of the Japan Society for the Promotion of Science for Young Scientists (Y.U. & N.I.).

References

[1] Formaggio, F., Bonchio, M., Crisma, M., Peggion, C., Mezzato, S., Polese, A., Barazza, A., Antonello, S., Maran, F., Broxterman, Q. B., Kaptein, B., Kamphuis, J., Vitale, R. M., Saviano, M., Benedetti, E., & Toniolo, C. (2002). *Chem. Eur. J.*, *8*, 84.

[2] Hubbell, W. L. & McConnell, H. M. (1971). *J. Am. Chem. Soc.*, *93*, 314.

[3] Matsumoto, K., Hyogo, F., Matsumoto, A., Koretsky, A., Sowers, A. L., Mitchell, J. B., & Krishna, M. C. (2006). *Clin. Cancer Res.*, *12*, 2455.

[4] He, G., Samouilov, A., Kuppusamy, P., & Zweier, J. L. J. (2001). *Magn. Reson.*, *148*, 155.

[5] Mitchell, J. B., Xavier, S., DeLuca, A. M., Sowers, A. L., Cook, J. A., Krishna, M. C., Hahn, S. M., & Russo, A. (2003). *Free Radic. Boil. Med.*, *34*, 93.

[6] Bilski, P., Hideg, K., Kalai, T., Bilska, M. A., & Chignell, C. F. (2003). *Free. Radic. Biol. Med.*, *34*, 489.

[7] Aurich, H. G. (1989). In: *Nitrones, Nitrorates and Nitroxides*, Patai, S. & Rappoport, Z. (Eds.), John Wiley & Sons: New York, 313.
[8] Ikuma, N., Tamura, R., Shimono, S., Kawame, N., Tamada, O., Sakai, N., Yamauchi, J., & Yamamoto, Y. (2004). *Angew. Chem. Int. Ed.*, *43*, 3677.
[9] Ikuma, N., Tamura, R., Shimono, S., Uchida, Y., Masaki, K., Yamauchi, J., Aoki, Y., & Nohira, H. (2006). *Adv. Mater.*, *18*, 477.
[10] Ikuma, N., Tamura, R., Shimono, S., Masaki, K., Uchida, Y., Yamauchi, J., Aoki, Y., & Nohira, H. (2006). *Ferroelectrics*, *343*, 119.
[11] Uchida, Y., Tamura, R., Ikuma, N., Yamauchi, J., Aoki, Y., & Nohira, H. (2007). *Mol. Cryst. Liq. Cryst.*, *479*, 213.
[12] Uchida, Y., Tamura, R., Ikuma, N., Yamauchi, J., Aoki, Y., & Nohira, H. (2008). *Ferroelectrics*, *365*, 158.
[13] Uchida, Y., Suzuki, K., Tamura, R., Aoki, Y., & Nohira, H. (2013). *J. Phys. Chem. B*, *117*, 3054.
[14] Einhorn, J., Einhorn, C., Ratajczak, F., Gautier-Lunear, I., & Pierre, J.-L. (1997). *J. Org. Chem.*, *62*, 9385.
[15] Kalai, T., Jeko, J., Hubbell, W. L., & Hideg, K. (2003). *Synthesis*, 2084.
[16] Ikuma, N., Tamura, R., Shimono, S., Kawame, N., Tamada, O., Sakai, N., Yamauchi, J., & Yamamoto, Y. (2003). *Mendeleev Commun.*, 109.
[17] Ikuma, N., Tamura, R., Shimono, S., Kawame, N., Tamada, O., Sakai, N., Yamamoto, Y., & Yamauchi, J. (2005). *Mol. Cryst. Liq. Cryst.*, *440*, 23.
[18] Ikuma, N., Tsue, H., Tsue, N., Shimono, S., Uchida, Y., Masaki, K., Matsuoka, N., & Tamura, R. (2005). *Org. Lett.*, *7*, 1797.
[19] Uchida, Y., Tamura, R., Ikuma, N., Masaki, K., Takahashi, H., Shimono, S., & Yamauchi, J. (2006). *Mendeleev Commun.*, *2*, 69.
[20] Li, X., Abell, C., & Ladlow, M. (2003). *J. Org. Chem.*, *68*, 4189.
[21] Vass, A., Dudas, J., Toth, J., & Varma, R. S. (2001). *Tetrahedron Lett.*, *42*, 5347.
[22] Kong, J., White, C. A., Krylov, A. I., Sherrill, C. D., Adamson, R. D., Furlani, T. R., Lee, M. S., Lee, A. M., Gwaltney, S. R., Adams, T. R., Ochsenfeld, C., Gilbert, A. T. B., Kedziora, G. S., Rassolov, V. A., Maurice, D. R., Nair, N., Shao, Y., Besley, N. A., Maslen, P. E., Dombroski, J. P., Daschel, H., Zhang, W., Korambath, P. P., Baker, J., Byrd, E. F. C., Van Voorhis, T., Oumi, M., Hirata, S., Hsu, C.-P., Ishikawa, N., Florian, J., Warshel, A., Johnson, B. G., Gill, P. M. W., Head-Gordon, M., & Pople, J. A. (2000). *J. Comput. Chem.*, *21*, 1532.
[23] Walba, D. M., Slater, S. C., Thurmes, W. N., Clark, N. A., & Handschy, M. A. (1986). *J. Am. Chem. Soc.*, *108*, 5210.
[24] Ajayaghosh, A. & Praveen, V. K. (2007). *Acc. Che. Res.*, *40*, 644.
[25] Kaszynski, P. (1999). In: *Magnetic Properties of Organic Molecules*, Lahti, P. M. (Ed.), Marcel Dekker: New York, 305.
[26] Mieda, Y., Hoshi, H., Takanishi, Y., Takezoe, H., & Zeks, B. (2003). *Phys. Rev. E*, *67*, 021701–1.

Appendix: Crystal structure of (±)-**1a** (Fig. A1), DSC curves (Fig. A2) and crystallographic data for (±)-**1a** (Table A1).

Appendix A. Table A1. Crystallographic Data for (±)-**1a**

structure formula	$C_{33}H_{41}O_3N_2$
formula weight	513.70
crystal dimensions (mm)	0.30 × 0.30 × 0.20
crystal system	Monoclinic
space group	*C*2/*c*
a (Å)	24.660(2)
b (Å)	11.8753(8)
c (Å)	20.4163(14)
β (°)	107.214(3)
vol (Å^3)	5710.9(7)
Z	8
ρ_{calc} (g/cm^3)	1.197
$2\theta_{max}$ (°)	55.0
radiation	MoKα
wavelength (Å)	0.71075
scan mode	ω
temp (K)	173
number of measured reflections	27222
number of independent reflections	6551
number of reflections included in the refinement	6996
σ limits	$I > 2.00\sigma(I)$
μ (cm^{-1})	0.759
method of structure solution	Direct Method (SIR97)
method of refinement	Full-matrix least-square on F^2
number of parameters	373
Goodness-of-fit on F^2	0.982
*R*1	0.096
*wR*2	0.239
maximum peak in final diff. map (e$^-$/Å^3)	1.16
minimum peak in final diff. map (e$^-$/Å^3)	1.00

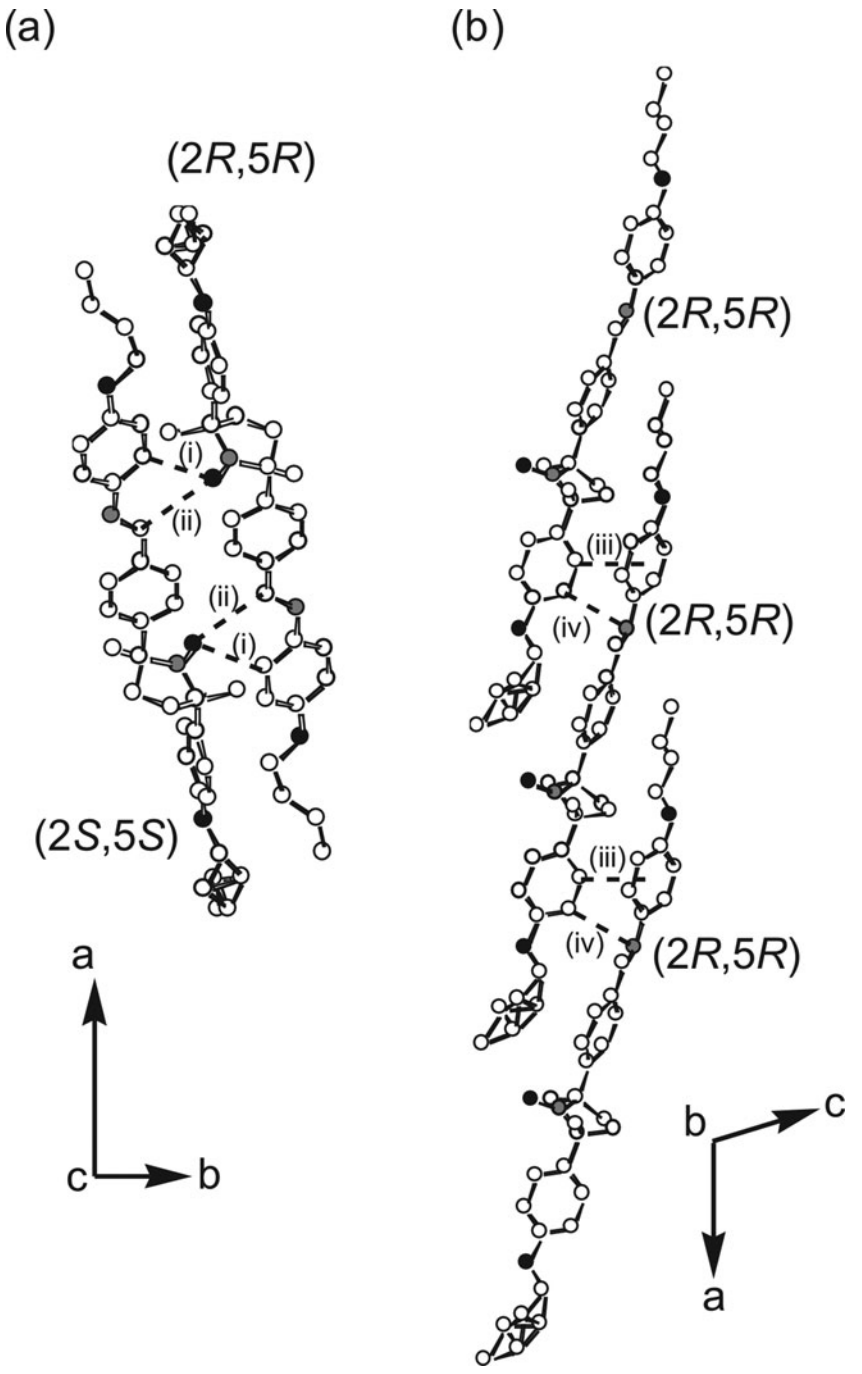

Figure A1. Crystal structure of (±)-**1a**: (a) a heterochiral dimer on the *bc* plane containing two kinds of CH/O interactions; C—O distance, (i) 3.55 Å and (ii) 3.33 Å. (b) a homochiral 1D chain along the *a* axis containing CH/π interactions [C—phenyl centroid distance, (iii) 3.55 Å] and CH/N interactions [C—N distance, (iv) 3.58 Å]. Carbon, oxygen and nitrogen atoms are denoted by white, gray, and black circles, respectively.

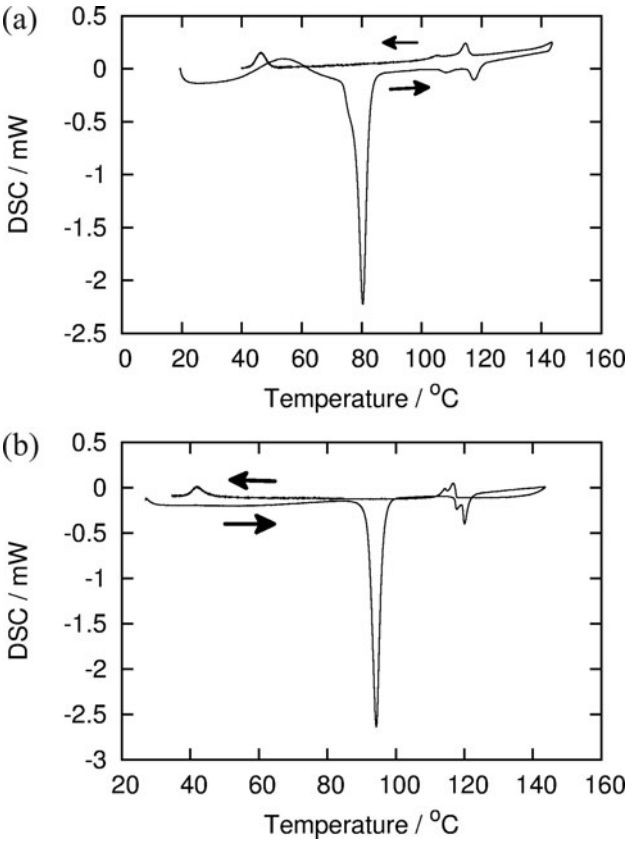

Figure A2. DSC curves of (a) (2*S*,5*S*)-**1f** and (b) (2*S*,5*S*)-**1g**.